

Epitaxial Templating of Two-Dimensional Metal Chloride Nanocrystals on Monolayer Molybdenum Disulphide

Shanshan Wang¹, Huashan Li², Junying Zhang,³ Shiaoqiang Guo,³ Wenshuo Xu,¹ Jeffrey C. Grossman², Jamie H. Warner^{1}*

¹Department of Materials, University of Oxford, Parks Road, Oxford, OX1 3PH, United Kingdom

²Department of Materials Science and Engineering, Massachusetts Institute of Technology, 77 Massachusetts Avenue, Cambridge, MA, 02139, USA.

³Key Laboratory of Micro-nano Measurement, Manipulation and Physics (Ministry of Education), Department of Physics, Beihang University, Beijing 100191, P. R. China

*Jamie.warner@materials.ox.ac.uk;

Abstract

We demonstrate the formation of ionic metal chloride (CuCl) two-dimensional (2D) nanocrystals epitaxially templated on the surface of monolayer molybdenum disulphide (MoS₂). These 2D CuCl nanocrystals are single atomic planes from a non-layered bulk CuCl structure. They are stabilized as a 2D monolayer on the surface of the MoS₂ through interactions with the uniform periodic surface of the MoS₂. The heterostructure 2D system is studied at the atomic level using aberration

corrected transmission electron microscopy (AC-TEM) at 80kV. Dynamics of discrete rotations of the CuCl nanocrystals are observed, maintaining two types of preferential alignments to the MoS₂ lattice, confirming the strong interlayer interactions drive the stable CuCl structure. Strain maps are produced from displacement maps and used to track real time variations of local atomic bonding and defect production. Density functional theory (DFT) calculations interpret the formation of two types of energetically advantageous commensurate superlattices *via* strong chemical bonds at interfaces, and predict their corresponding electronic structures. These results show how vertical heterostructured 2D nanoscale systems can be formed beyond the simple assembly of preformed layered materials and provide indications about how different 2D components and their interfacial coupling could influence the overall property of the heterostructures.

KEYWORDS: MoS₂, 2D crystal, metal chloride, vertical heterostructure, AC-TEM, epitaxy

The successful isolation of individual graphene layers sparked a surge in the exploration of other 2D crystals, such as hexagonal boron nitride (h-BN) and transition metal dichalcogenides (MoS₂, WS₂, *etc.*).^{1–5} With the enrichment of various kinds of 2D materials, interest has been extended to the artificial assembly of different atomically thin layers to form van der Waals heterostructures.⁶ To date, typical vertical layered heterostructures (VLHs), including graphene/h-BN,^{7,8} MoS₂/graphene,^{9–11} MoS₂/h-BN^{12,13} and MoS₂/WS₂,^{14–16} have been fabricated through either sequential mechanical transfer or direct growth using chemical vapor deposition (CVD). The 2D building blocks are generally layered atomic crystals in bulk form with strong covalent bonds in-plane and weak interlayer van der Waals interactions, which facilitates the isolation into monolayer films and then the vertical stacking into hybrid 2D heterostructures. The interlayer interactions in VLHs depend not only on the two materials, but also the relative orientation of the

lattice directions in each layer. Lattice alignment between neighboring 2D crystals forms heteroepitaxial bilayers with surface reconstruction, interfacial charge transfer and proximity effects such as Coulomb interactions and quantum tunneling.^{17–22} Yang *et al.* showed the epitaxial growth of single-domain graphene on h-BN using a plasma-assisted deposition approach, which induced a second Dirac point to appear.¹⁷ Gong *et al.* reported the synthesis of epitaxially-stacked WS₂/MoS₂ heterostructures by a vapor phase growth at high temperature (~850°C), which generated a strong interlayer exciton transition due to the type-II band alignment.¹⁴

The ability to extend vertical heterostructures by using materials that are not typically layered systems would further expand the variety of options for material choice and ultimately control over the desired properties. Recent research using aberration corrected (scanning) transmission electron microscopy (AC-(S)TEM) has shown that a 2D material template can help the stabilization and crystallization of non-layered materials into a 2D form. Qu *et al.* showed the epitaxial growth of 2D crystalline gold nanocrystals on graphene at elevated temperatures.²³ Al Balushi *et al.* reported the growth of 2D gallium nitride (GaN) on the bulk 6H-SiC substrate with the help of graphene encapsulation.²⁴ However, the achievement of 2D non-layered materials is still lacking with limited understanding about the interfacial interactions between the 2D layered and non-layered material. In addition, they commonly adopt a similar crystal symmetry in the stacking plane, making people know little about whether non-layered materials having a different lattice symmetry from the layered template can also be stabilized in a 2D form. Recently 2D suspended Fe within graphene nanopores and 2D layered ZnO nanocrystals on graphene have been produced.^{25,26} Moreover, expanding the underlying 2D template beyond graphene, such as using monolayer transition metal dichalcogenides is highly desirable, which would provide opportunities to create exotic mixed 2D hybrid semiconductor systems with distinct fundamental physics.

Metal chlorides offer a wide range of compounds and have been frequently used to dope graphene in the form of FeCl_2 to lower its sheet resistance for electronic applications, indicating strong interactions with the hexagonal 2D lattice structure. However, semiconducting metal chlorides are more promising for VLHs with monolayer TMDs due to possibility of forming heterostructures with distinct excitonic states. CuCl is a I-VII compound with ionic character and adopts a wide direct bandgap, similar in energy to GaN and ZnO . The cubic zinc-blende structure is the most thermodynamically preferable and commonly seen form with a wide direct band gap of 3.4 eV²⁷ and a large exciton binding energy (190 meV for the Z_3 exciton) (Supporting Information Figure S1).²⁸ It is comprised of two interpenetrating face-centered-cubic (FCC) unit cells occupied by Cu and Cl, respectively, which can be seen as a binary diamond crystal structure. For a CuCl crystal which is in one-unit-cell thickness, it possesses only 4 atomic layers with each atomic column having only one atom, either Cu or Cl, from the view along [001] direction (Note that atoms sitting at the top and bottom faces of the unit cell can only be considered as half an atom because they need to be shared with neighbors). It also has a large dipole moment, because Cu and Cl atoms with opposite charges are arranged in different atomic layers stacked alternatively. Since 2D CuCl and monolayer MoS_2 are seen as the analogue of diamond and graphene, respectively, fabricating 2D CuCl on monolayer MoS_2 will realize the achievement of ‘diamond-graphene-like’ 2D vertical heterostructures, in which two 2D building blocks possess distinct and typical crystal symmetries. The generation of this vertical heterostructures will provide fundamental knowledge to help expand the library of 2D materials further and understand the evolution of the overall properties after coupling different 2D blocks together.

Here, we show that monolayer 2D CuCl nanocrystals can easily form on the surface of monolayer MoS_2 . The CuCl phase observed is a bulk 3D material, not a layered system, and its

formation into a monolayer sheet is driven by the underlying epitaxial interactions with the MoS₂. These CuCl 2D crystals are formed *in-situ* within an AC-TEM, by electron beam decomposition of solution deposited CuCl₂ precursor material that resides on the surface of MoS₂. Two preferred epitaxial orientations of 2D CuCl on monolayer MoS₂ have been observed with DFT-relaxed models showing the detailed coupling mode at the interface. We image the atomic positions of the CuCl atoms within the nanocrystals to accurately determine the crystal structure and also track the real-time dynamics of CuCl nanocrystals as they undergo phase changes and rotations, providing insights into the epitaxial correlations to the underlying MoS₂ lattice. 2D displacement and strain maps are generated to quantitatively investigate the lattice distortion in 2D CuCl nanocrystals. The electronic structure of two types of heteroepitaxial structures of CuCl/MoS₂ are provided by DFT calculations, indicating that both electronic and spintronic properties may be substantially affected by the orbital hybridization *via* chemical bonding and intrinsic dipole moment in CuCl nanocrystals.

Results and Discussion

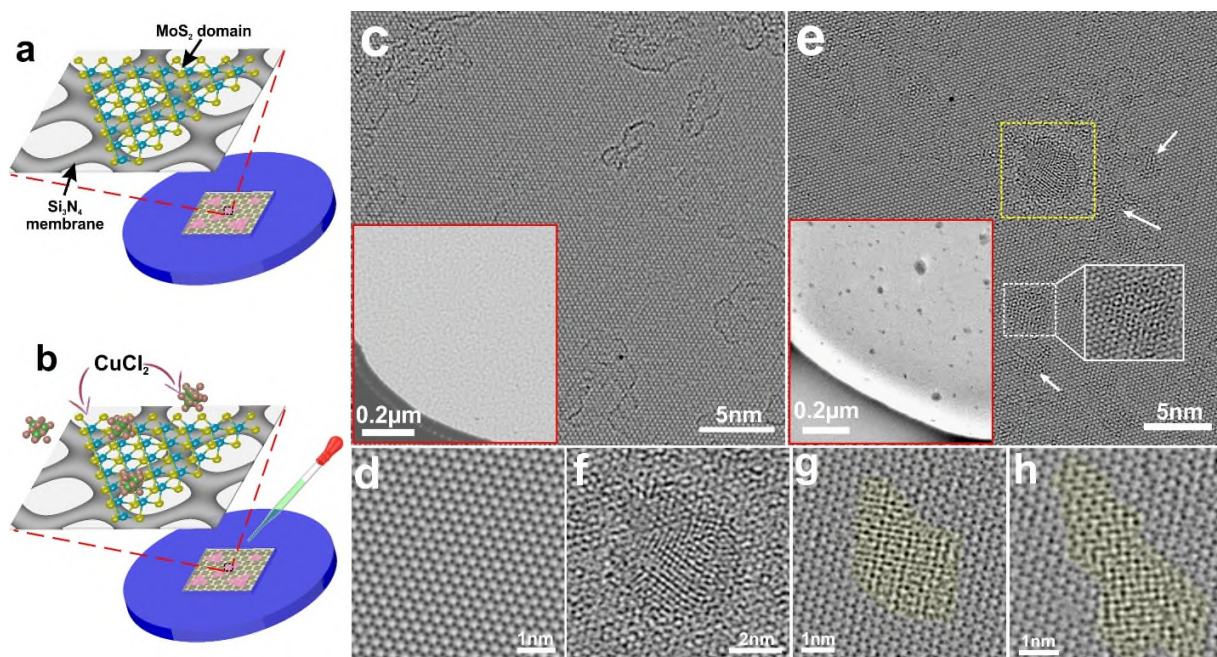


Figure 1. (a,b) Schematic illustrations showing the transfer of monolayer MoS₂ onto the Si₃N₄ TEM grid (a) followed by doping MoS₂ films with copper(II) chloride (CuCl₂) solution through a drop-casting procedure (b). (c) Medium-magnification AC-TEM image of a pristine monolayer MoS₂ film before CuCl₂ deposition. Inset is the low-magnification AC-TEM image of the same area. (d) High-magnification AC-TEM image of intrinsic MoS₂ monolayers. (e) Medium-magnification AC-TEM image of a pristine monolayer MoS₂ film doped by CuCl₂, where exotic nanocrystals (yellow dashed box) with thin amorphous substances surrounded (white dashed box and white arrows) can be seen on the surface. Inset on the left bottom box is the low-magnification TEM image of the same area showing the attachment of small nanoparticles on MoS₂ surface. (f) Magnified AC-TEM image of the yellow boxed region in Figure 1e. (g-h) High-magnification AC-TEM images showing cubic 2D CuCl nanocrystals grown on monolayer MoS₂ with two typical preferential orientations after electron beam irradiation (white dashed box and white arrows in Figure 1e). Different moiré patterns are seen, as highlighted by semitransparent yellow masks, indicating various lattice correlations between 2D CuCl and single layer MoS₂ lattice points.

Monolayer MoS₂ was synthesized by chemical vapor deposition (CVD) method similar to previous work and transferred to Si₃N₄ TEM grids with 2 μm holes (Figure 1a).²⁸ Both the low-magnification and high resolution TEM images confirm the clean MoS₂ surface with only small regions covered by typical amorphous carbon residue (Figure 1c). The AC-TEM image in Figure 1d shows the hexagonal lattice structure of pristine monolayer MoS₂ with atomic resolution. One drop of 0.05 M copper (II) chloride (CuCl₂) in ethanol solution was deposited onto MoS₂ (Figure 1b) and allowed to dry in air, leading to the formation of a nanoparticles with diameters of several nanometers on the MoS₂ surface (Figure 1e). The large three-dimensional nanocrystals (Figure 1f) are easily observed during AC-TEM, but examination of the area also revealed thin amorphous CuCl₂ material was present, with lower contrast than the larger nanocrystals. Electron beam irradiation of the amorphous CuCl₂ region resulted in the transformation to a crystalline phase (Supporting Information Figure S19). Characterization of the crystalline structure revealed they are predominantly 2D copper (I) chloride (CuCl) nanocrystals in the cubic zincblende structure. The CuCl nanocrystals adopt epitaxial orientations with the underlying monolayer MoS₂ (Figure 1g,h, Supporting Information Figure S2–S9).

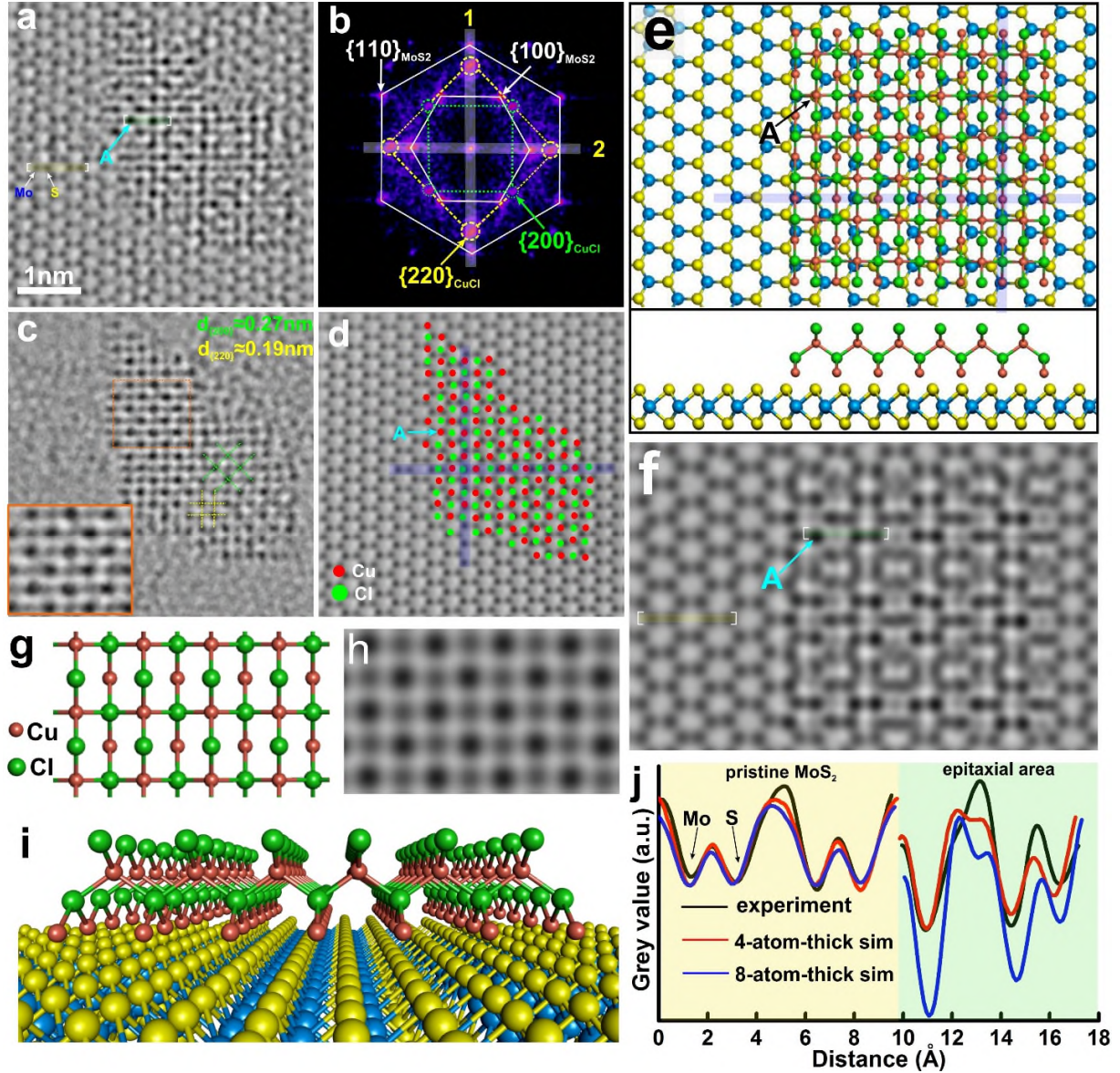


Figure 2. (a) AC-TEM image showing a typical example 2D cubic CuCl on monolayer MoS₂ with Type-I relative heteroepitaxy. (b) 2D Fast Fourier Transform (FFT) of (a). Aligned spots between CuCl and MoS₂ are marked by two half-transparent white lines, 1 and 2, respectively. (c) Reconstructed AC-TEM image after applying a mask to 2D FFT of (b) to remove the MoS₂ lattice contribution, showing only the 2D CuCl lattice structure. Inset is the magnified image of the orange boxed region. Yellow and green dashed lines label out the lattice planes of {200} and {220} of this 2D CuCl nanocrystal, respectively. (d) Image showing the atomic positions of the Cu and Cl atoms relative to the monolayer MoS₂ template (see Methods). Purple

lines indicate two different lattice plane directions belonging to $\{220\}_{\text{CuCl}}$ are aligned with one zigzag and one armchair direction of monolayer MoS_2 , respectively. (e) Atomic model based on the analysis from (b) and (d), shown in top view that represents the projection seen by AC-TEM. Two purple lines indicate the two main lattice alignment relationship between 2D CuCl and MoS_2 . The side view is placed in the bottom part. The model of 2D CuCl is from its intrinsic bulk counterparts. (f) Multislice TEM image simulation based on the atomic model in (e). (g) Isolated 2D CuCl model after removing the bottom monolayer MoS_2 lattice in (e). (h) Multislice TEM image simulation based on (g). (i) 3D perspective side view of the model in (e) showing the CuCl structure. (j) Line profiles comparing the atomic column intensities from the experimental and simulated images, respectively (see Methods).

Figure 2a shows the AC-TEM image of 2D cubic zincblende CuCl on MoS_2 in a ‘Type-I’ heteroepitaxial orientation that results in a specific moiré pattern. 2D FFT of Figure 2a shows four sets of spots: two sets which are in hexagonal pattern can be assigned to $\{100\}$ and $\{110\}$ of monolayer MoS_2 , representing zigzag and armchair directions, respectively, while the other two sets which are in the squared pattern belong to $\{200\}$ and $\{220\}$ of 2D CuCl . According to the CuCl lattice configuration, $\{220\}$ of CuCl ($\{220\}_{\text{CuCl}}$) adopts two different crystal directions, which are perpendicular to each other (orange dashed lines in Supporting Information Figure S1c). One crystal direction of $\{220\}_{\text{CuCl}}$ is aligned with one armchair direction of MoS_2 , while the other lattice plane orientation of $\{220\}_{\text{CuCl}}$ is parallel to one zigzag direction of MoS_2 , as indicated by two semitransparent white columns in Figure 2b. This crystallographic relationship between heteroepitaxial 2D CuCl and the template monolayer MoS_2 can be defined as $(001)_{\text{CuCl}} // (001)_{\text{MoS}_2}$; $[110]_{\text{CuCl}} // [110]_{\text{MoS}_2}$. The lattice structure of 2D CuCl can be extracted by applying a mask to the 2D FFT to filter out the lattice contribution from monolayer MoS_2 (Figure 2c). 2D CuCl has a squared lattice periodicity from the projective view with dark and bright spots arranged alternatively, indicating its thickness to be the integral multiples of 4 atomic layers, equaling to

one-unit-cell thickness of the bulk CuCl crystal (Supporting Information Figure S10). The interplanar spacing of $\{200\}_{\text{CuCl}}$ and $\{220\}_{\text{CuCl}}$ are measured to be ~ 0.27 nm and ~ 0.19 nm, respectively, which is consistent with that for bulk CuCl (Supporting Information Figure S1e). The d-spacing of $\{200\}_{\text{CuCl}}$ has a good match with that of $\{100\}_{\text{MoS}_2}$, which may contribute to the formation and stability of this heteroepitaxial structure. Figure 2d shows the absolute location for each Cu and Cl atom from 2D CuCl on the monolayer MoS₂ lattice in the real space, which confirms the crystal plane alignment relation based on the 2D FFT in Figure 2b. For the construction of the atomic model for Type-I CuCl/MoS₂ heterostructures, a point, where the Cu atom from 2D CuCl and the double S atoms from monolayer MoS₂ are almost perfectly eclipsed, was found in Figure 2d, marked as ‘A’. It is chosen as a reference point to determine the absolute position between the 2D CuCl atomic model and the monolayer MoS₂ model, thus obtaining the atomic model shown in Figure 2e. The 3D perspective view of the model (Figure 2i) highlights the non-planar configuration of 2D cubic CuCl lattice. The multislice TEM simulation generated based on this atomic model agrees with the AC-TEM image and shows a ‘brick-wall-like’ moiré pattern at the epitaxial region (Figure 2f) similar as the AC-TEM image (Figure 2a). We also did the TEM image simulation based on the individual 2D CuCl atomic model (Figure 2g), which provides a similar squared lattice configuration in the top view, agreeing well with the reconstructed AC-TEM image of CuCl (inset of Figure 2c). To determine the thickness of CuCl, we compared the relative intensity variations between monolayer MoS₂ and the typical structures in the heteroepitaxial regions for both the experimental AC-TEM image and the image simulations with different 2D CuCl thickness (Figure 2i). It is confirmed that the CuCl is only 4-atom-thick (equaling to one-unit-cell-thick in bulk CuCl) having only one atom, either Cu or Cl, in each atomic column from the projection view (Figure 2e).

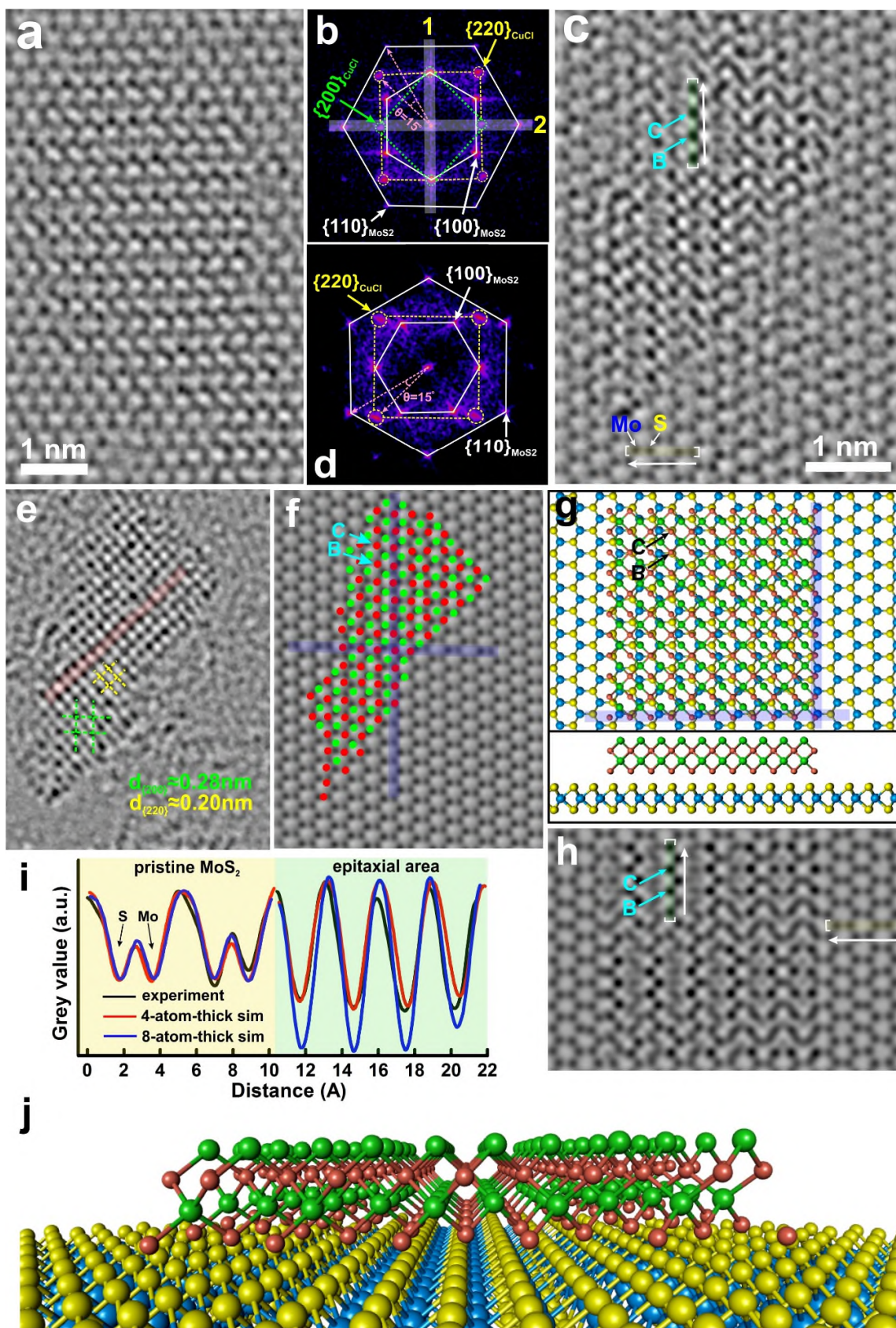


Figure 3. (a) AC-TEM image of one typical example of Type-II heteroepitaxy mode between 2D CuCl and monolayer MoS₂. (b) 2D FFT of (a). (c) AC-TEM image of another typical example of Type-II heteroepitaxy mode captured at a different defocus from that of Figure 3a. (d) 2D FFT of (c). (e) Reconstructed AC-TEM image after applying a mask to (d) to filter out MoS₂ lattice contribution. (f) Image showing the atomic positions of Cu and Cl atoms from CuCl relative to the monolayer MoS₂ template. Purple lines indicate that two different lattice plane directions belonging to {200}_{CuCl} are aligned with one zigzag and one armchair direction of monolayer MoS₂, respectively. (g) Atomic model based on the analysis from (d) and (f) with both the projective (top panel) and side (bottom panel) view. (h) Multislice TEM image simulation corresponding to the atomic model in (g). (i) Line profiles comparing the atomic column intensities from the experimental and simulated images, respectively (see Method). (j) 3D perspective side view of the model in (g).

Figure 3a shows an AC-TEM of the Type-II heteroepitaxy between 2D CuCl and monolayer MoS₂. 2D FFT shows that two different crystal directions of {200}_{CuCl}, which are perpendicular to each other, are aligned to one zigzag and one armchair orientation of MoS₂, respectively, as indicated by two white semitransparent lines in Figure 3b. The crystallographic relation for this Type-II heteroepitaxy can be expressed as (001)_{CuCl} // (001)_{MoS₂}; [100]_{CuCl} // [110]_{MoS₂}. Since the interplanar spacing of {200}_{CuCl} and {100}_{MoS₂} are very close, two reflexes covered by line ‘1’, which correspond to the crystal planes from {200}_{CuCl} and {100}_{MoS₂}, respectively, overlap with each other. According to the geometric relations between the cubic CuCl and hexagonal MoS₂ lattice, the smallest intersection angle between two crystal faces from {220}_{CuCl} and {110}_{MoS₂}, is 15° in the Type-II heteroepitaxy, as marked by the angle θ between two pink arrows in Figure 3b.

Figure 3c is another typical example of Type-II heteroepitaxy but is captured at a different defocus. This results in the low visibility of reflexes corresponding to {200}_{CuCl} (Figure 3d).

However, we are still able to determine the stacking orientation between CuCl and MoS₂ by measuring θ , and confirm this epitaxial mode to be also Type-II. The 2D CuCl crystal is individually shown in Figure 3e after removing the signal contribution from MoS₂ lattice. The atom contrast between two neighboring atomic positions is more uniform compared with Figure 2c, without a distinct light and dark alternation in brightness. This may arise from a different defocus value for 2D CuCl lattice under this imaging condition, which also results in a decreased intensity of $\{200\}_{\text{CuCl}}$ reflexes in 2D FFT (Figure 3d, Supporting Information Figure S11). The interplanar spacing for $\{220\}_{\text{CuCl}}$ is measured to be $\sim 0.20\text{nm}$ by using reflexes from monolayer MoS₂ in 2D FFT as the reference. Therefore, we can deduce the d-spacing of $\{200\}_{\text{CuCl}}$ to be approximately 0.28 nm based on the CuCl crystal structure. The lattice parameters for 2D CuCl in Type-I and Type-II heteroepitaxial modes show a good consistence with each other with a small error, which could derive from either measurements or tiny TEM image distortion. An obvious increase on the structural disorder, revealed as the lattice distortion marked by a red strip in Figure 3e, can be observed in 2D CuCl crystal. Such loss of structural coherence will be quantitatively analyzed by generating 2D strain maps in Figure 6. The position of each atoms from 2D CuCl on monolayer MoS₂ are shown in Figure 3f, demonstrating the crystal direction alignment between two perpendicular orientations from $\{200\}_{\text{CuCl}}$ and the MoS₂ zigzag and armchair directions, as highlighted by two purple lines. The atomic model is generated in Figure 3g from the view angle along the yellow arrow in Figure 3c. The corresponding multislice TEM simulation (Figure 3h) exhibits the same ‘leaf-like’ moiré pattern as the experimental image (Figure 3c). The intensity line profiles between the pristine monolayer MoS₂ and the typical epitaxial region for both experimental image and the simulations confirms the 4-atom-thickness of the 2D CuCl crystal in this example, which is consistent with Type-I CuCl/MoS₂ heterostructures.

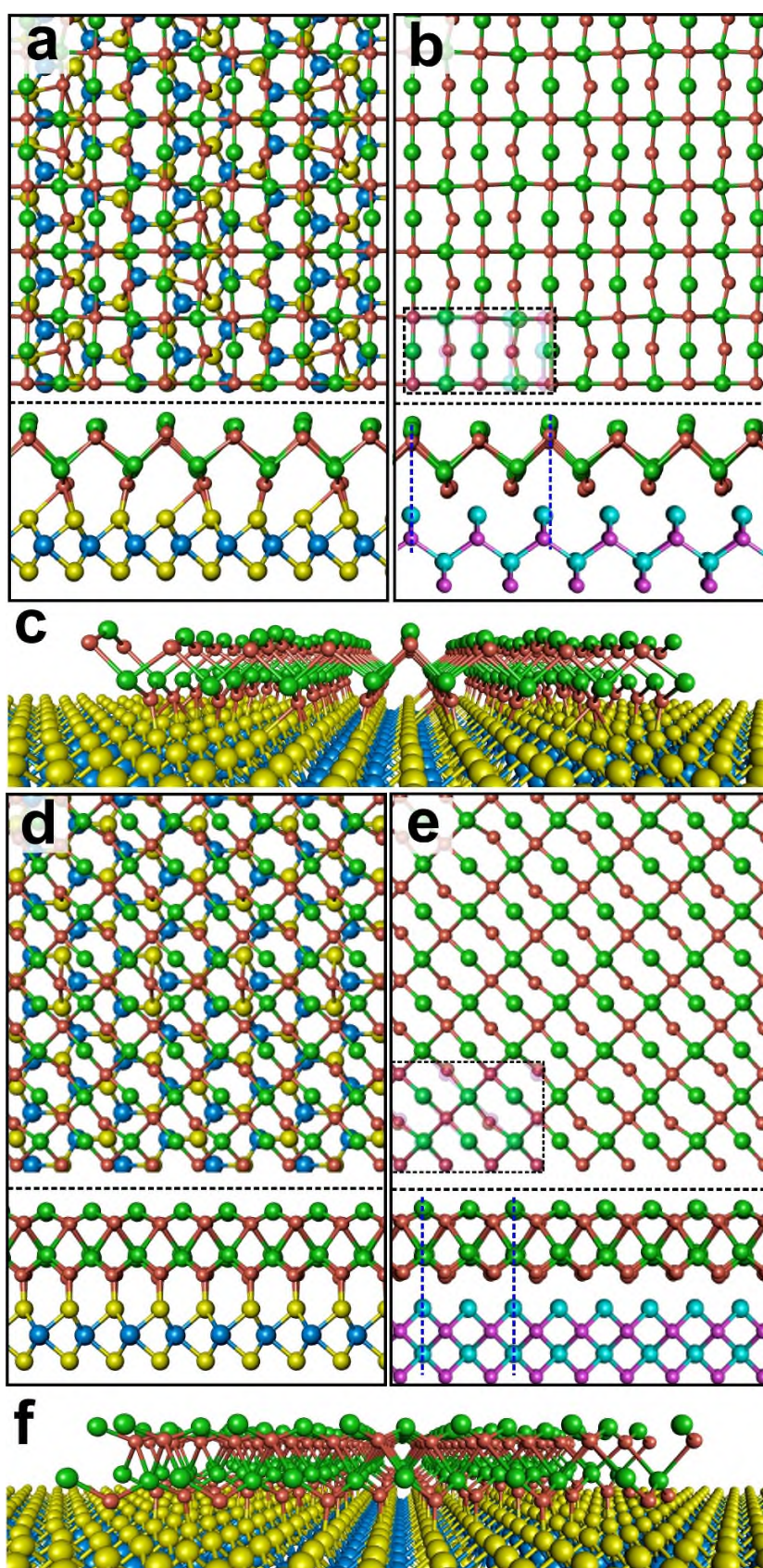


Figure 4. DFT-relaxed atomic model of Type-I (a) and Type-II (d) CuCl/MoS₂ heterostructures with both the projective view and the side view. The monolayer MoS₂ template is removed to show the 4-atom-thick CuCl atomic model separately in Type-I (b) and Type-II (e) heteroepitaxy. The unrelaxed cubic zincblende CuCl atomic model, having Cu and Cl atoms colored in pink and cyan, respectively, is placed at the bottom of the side view, which is used as a comparison to show the lattice distortion before and after the DFT relaxation. The dashed black box in the top panel of (b) and (e) overlaps a semitransparent unrelaxed CuCl model on the DFT-relaxed one to show the structural deformation of CuCl in the projection view. 3D perspective views of Type-I (c) and Type-II (f) CuCl/MoS₂ heterostructures are also provided.

DFT calculations were conducted to achieve the relaxed atomic model of CuCl/MoS₂ heterostructures in Type-I and Type-II epitaxy (Figure 4). The monolayer MoS₂ and the 4-atom-thick CuCl layer are mainly coupled *via* the strong Cu-S chemical bonding rather than weak van der Waals (vdW) interactions due to a high reactivity of unsaturated Cu atoms at the interface. This indicates that there exists a strict requirement about the position matching between Cu and S atoms in 2D CuCl/MoS₂ to enable a periodic bonding pattern for the establishment of the commensurate superlattice. This is different to previously studied 2D van der Waals heterostructures, which have a high tolerance on the lattice mismatch at the interface. Since monolayer MoS₂ has higher rigidity than 2D CuCl, it triggers a substantial lattice distortion in CuCl with MoS₂ barely perturbed. It is found that the 2D CuCl can adopt several equivalent or similar ground-state structures at such a symmetric interface and the energy barrier for the structure transition from one to another is low. Given the intrinsic flexibility of 2D CuCl and the energy injected by the electron beam, the atomic configuration of 2D CuCl may oscillate between different structural configurations during AC-TEM imaging. Therefore, the periodic square lattice in the projective view we observed in a AC-TEM image integrated over a single exposure (1–2 s) may be a time-averaged structure of 2D CuCl between several ground states. This phenomenon also

occurred in the TEM observation of the monovacancy in graphene.²⁹ We averaged over two DFT-relaxed equivalent structures with opposite in-plane polarized directions for Type-I and Type-II heteroepitaxy, respectively, and obtain the final averaged atomic configurations (Figure 4a,d, Supporting Information Figure S12) with their corresponding 3D perspective views (Figure 4c,f). After removing the bottom monolayer MoS₂, the separate 2D CuCl structure could be seen (Figure 4b,e), which preserves the square lattice geometry in the projective view well, consistent with the experimental observations, with slight in-plane distortion and a minor change on the lateral lattice spacing. The lattice deformation predominantly occurs in the direction perpendicular to the 2D membrane, as depicted by the side-view comparison between DFT-relaxed and unrelaxed CuCl atomic models in Figure 4b,e. The intensity line profiles between experimental AC-TEM images and image simulations based on corresponding averaged DFT-relaxed Type-I and Type-II heteroepitaxy models agree well with each other, indicating the validity of our deduction on the lattice configuration (Supporting Information Figure S13 and Figure S14). Despite the distinct stacking patterns and lattice mismatches (Supporting information Table S1), DFT calculations show that these two types of CuCl/MoS₂ interfaces have similar binding energies (type I: 0.47 eV, type II: 0.43 eV per unit of CuCl), which supports the hypothesis that the coupling between materials is primarily through chemical bonding rather than van der Waals forces. In addition, the interface structure is extremely sensitive to the choice of the supercell. Even a small deviation from the ideal situation leads to a significant amount of Cu-Cl bonds breaking and the ruin of the squared projective lattice structure (Supporting Information Figure S15). This further implies that the formation of ordered cubic-hexagonal interface relies on stringent material matching.

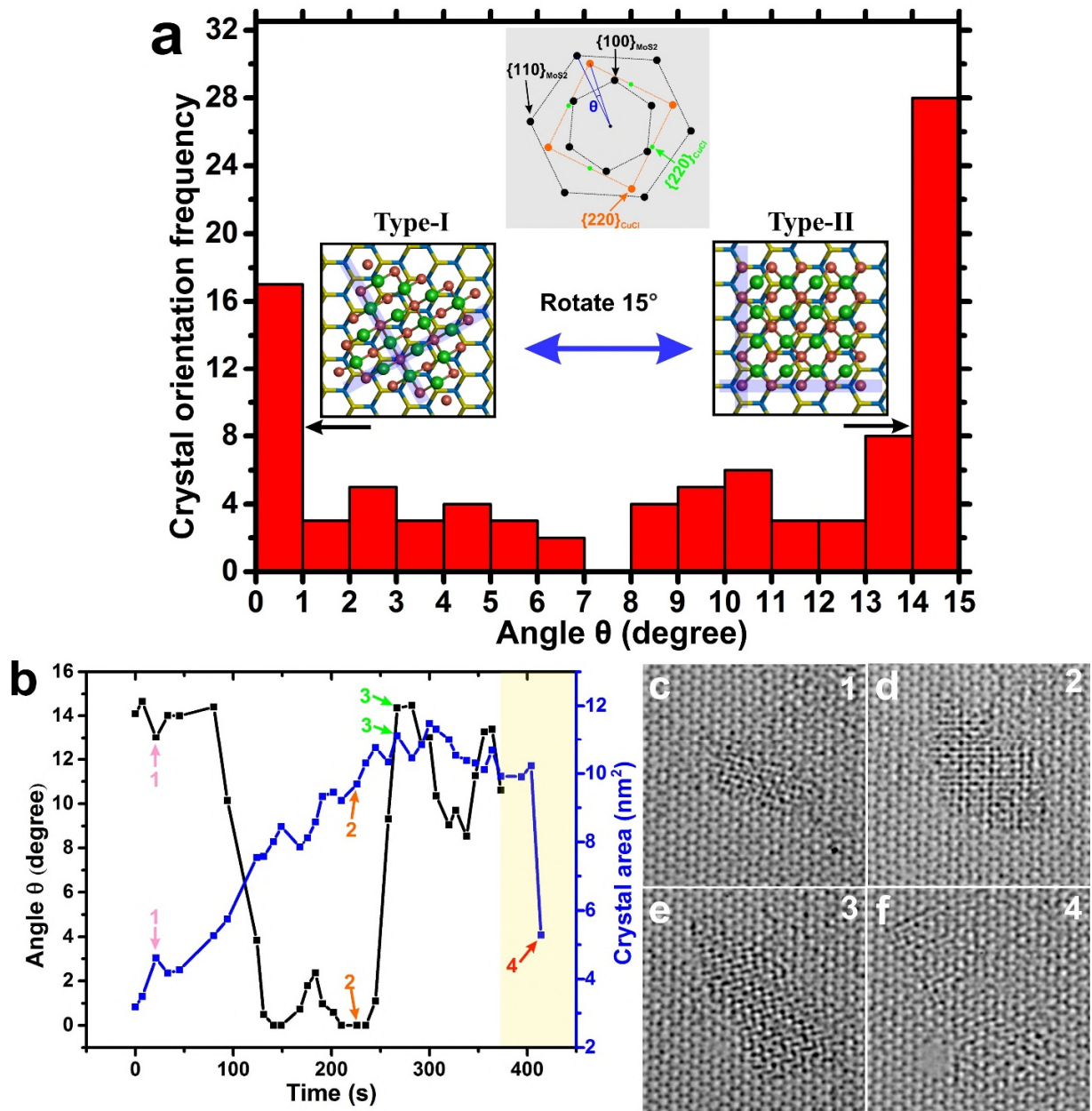


Figure 5. (a) Histograms showing the distribution of stacking orientation between 2D CuCl crystals and the monolayer MoS₂ template. (b) Plots showing the stacking orientation (black curve) and the area (blue curve) changes of one 2D CuCl crystal as a function of the exposure time under the electron beam. The yellow region indicates the time period when CuCl began to degrade. (c-f) Time-series of AC-TEM images showing this 2D CuCl crystal at four different time points, as marked by numbers 1 to 4 in (b). Figure 4d and e are the same as Figure 2a and 3c.

The stacking orientation distribution of 2D cubic CuCl on monolayer MoS₂ was investigated by analyzing the 2D FFT of more than 90 different AC-TEM frames (Figure 5a). As the schematic illustration of a typical 2D FFT of one CuCl/MoS₂ TEM image shown on the top panel of Figure 5a, we use the smallest intersection angle (θ) between one crystal direction of $\{220\}_{\text{CuCl}}$ and its closest one MoS₂ armchair direction to describe the stacking orientation between two films. Based on the symmetry relation between cubic CuCl and hexagonal MoS₂ crystals, two types of heteroepitaxial modes can transform to each other by rotating 15° (Supporting Information Figure S16). Therefore, Type-I heteroepitaxy corresponds to $\theta=0^\circ$, while Type-II heteroepitaxy corresponds to $\theta=15^\circ$. All the other stacking modes can be expressed by θ between 0° and 15° . By tracking one CuCl crystal from its birth to death, we found that it can rotate under the electron beam irradiation (Figure 5b) with approximately 50% of its lifetime adopting either Type-I ($0^\circ \leq \theta \leq 1^\circ$) or Type-II ($14^\circ \leq \theta \leq 15^\circ$) stacking orientations with respect to the MoS₂ template. This agrees with the statistical results in Figure 5a, where Type-I and Type-II heteroepitaxy yield a percentage of 18% and 30%, respectively, indicating an energetic preference for the crystal alignment strategy of these two epitaxial modes. Such epitaxial tendency between 2D CuCl and monolayer MoS₂ disappeared as CuCl nanocrystals became thicker, which might be induced by the reduced interfacial interactions of the template monolayer MoS₂ to the above CuCl (Supporting Information Figure S17). The blue curve in Figure 5b shows the area changes of the same 2D CuCl nanocrystal as a function of the observation time under the electron beam, which reveals the formation dynamics and the stability of this ultra-thin metal chloride nanocrystal. The formation of 2D CuCl starts from a small nucleation under the electron beam illumination, and then increases its area steadily followed by a level-off, which finally ends up with a sharp degradation. The lifespan of this CuCl under the electron beam illumination is more than 6 min,

indicating a relatively high stability of this 2D metal chloride nanocrystal templated on monolayer MoS₂ (Supporting Information Figure S20). Four AC-TEM images showing this 2D CuCl crystal at different stages are exhibited in Figure 5c–f.

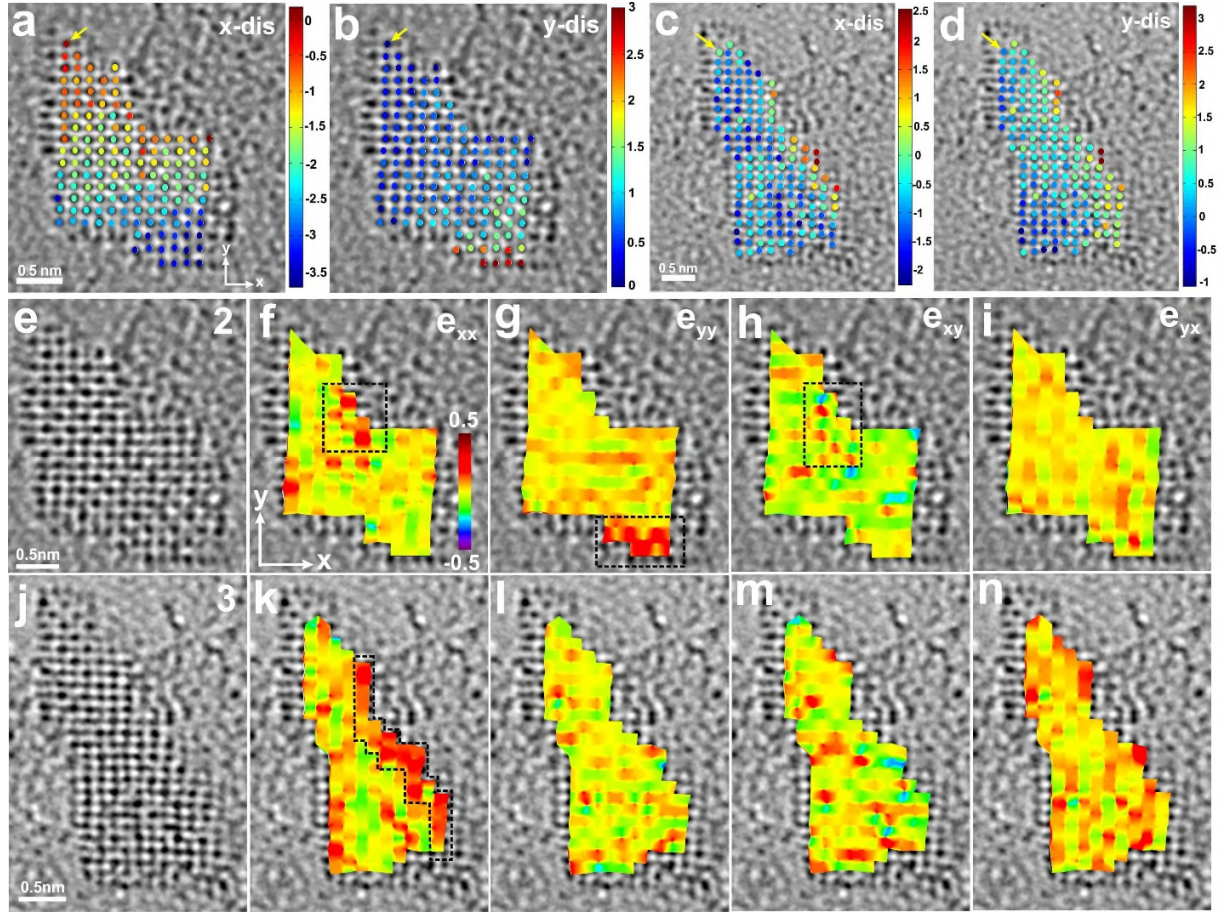


Figure 6. (a,b) 2D displacement maps in the x and y direction for 2D CuCl nanocrystal in (e). (c,d) 2D displacement maps in the x and y direction for 2D CuCl nanocrystal in (j). The unit of all color bars for displacement maps is Å. (e) Reconstructed AC-TEM image in Figure 5d showing the lattice structure of individual 2D CuCl nanocrystal at time point 2 after filtering out the signal contribution from monolayer MoS₂ lattice. The heteroepitaxial model between CuCl and MoS₂ is Type-I. (f-i) 2D strain maps of $\partial U_x/\partial x$, $\partial U_y/\partial y$, $\partial U_x/\partial y$, $\partial U_y/\partial x$ for 2D CuCl nanocrystal in (e). The color scale is ± 0.5 . (j) Reconstructed AC-TEM image in Figure 5e showing the individual 2D CuCl nanocrystal at time point 3. The heteroepitaxial

model between CuCl and MoS₂ is Type-II. (k-n) 2D strain maps of $\partial U_x/\partial x$, $\partial U_y/\partial y$, $\partial U_x/\partial y$, $\partial U_y/\partial x$ for 2D CuCl nanocrystal in (j). The color scale is ± 0.5 .

As depicted in Figure 3e, we observed an obvious structural disorder for 2D cubic zincblende CuCl nanocrystals compared with the intrinsic atomic model for its bulk counterparts. This increased structural incoherence is quantitatively studied by calculating the 2D strain field in CuCl lattice. Figure 6e and j show two reconstructed AC-TEM images based on Figure 5d and e showing 2D CuCl nanocrystals alone after filtering out the monolayer MoS₂ lattice. The heteroepitaxial model between 2D CuCl and the monolayer MoS₂ template in Figure 6e and j belongs to Type-I and Type-II, respectively. We examined the strain in these two 2D CuCl nanocrystals (Figure 6f-i, Figure 6k-n) from the displacement maps obtained by resolving the displacement values for each atom in the real space (Figure 6a-d, see Methods). It shows that the lattice periodicity of these ultrathin CuCl nanocrystals decreases with an increased level of random distortion in lattice and a broader distribution of bond length, as indicated by the 2D normal and shear strain maps in Figure 6. Such an increase of the structural disorder matches well with the DFT-calculated atomic models for 2D CuCl in both two types of heteroepitaxy (Figure 4b,e). The lattice irregularity could be triggered by the monolayer MoS₂ template, which adopts a different crystal symmetry compared with the 2D cubic zincblende CuCl nanocrystal. In addition, the high flexibility of ultrathin CuCl membrane and the strong chemical bonding at the CuCl/MoS₂ interface may further promote the structural disorder in 2D CuCl nanocrystals. It was also found that, atoms close to edges and corners of 2D CuCl sometimes suffer higher strains compared with the body region (black dashed boxes in Figure 6f- and Figure 6k-n), which might be due to diverse unsatisfied bonding environments at edges and corners and can drive an increased inhomogeneous internal strain.

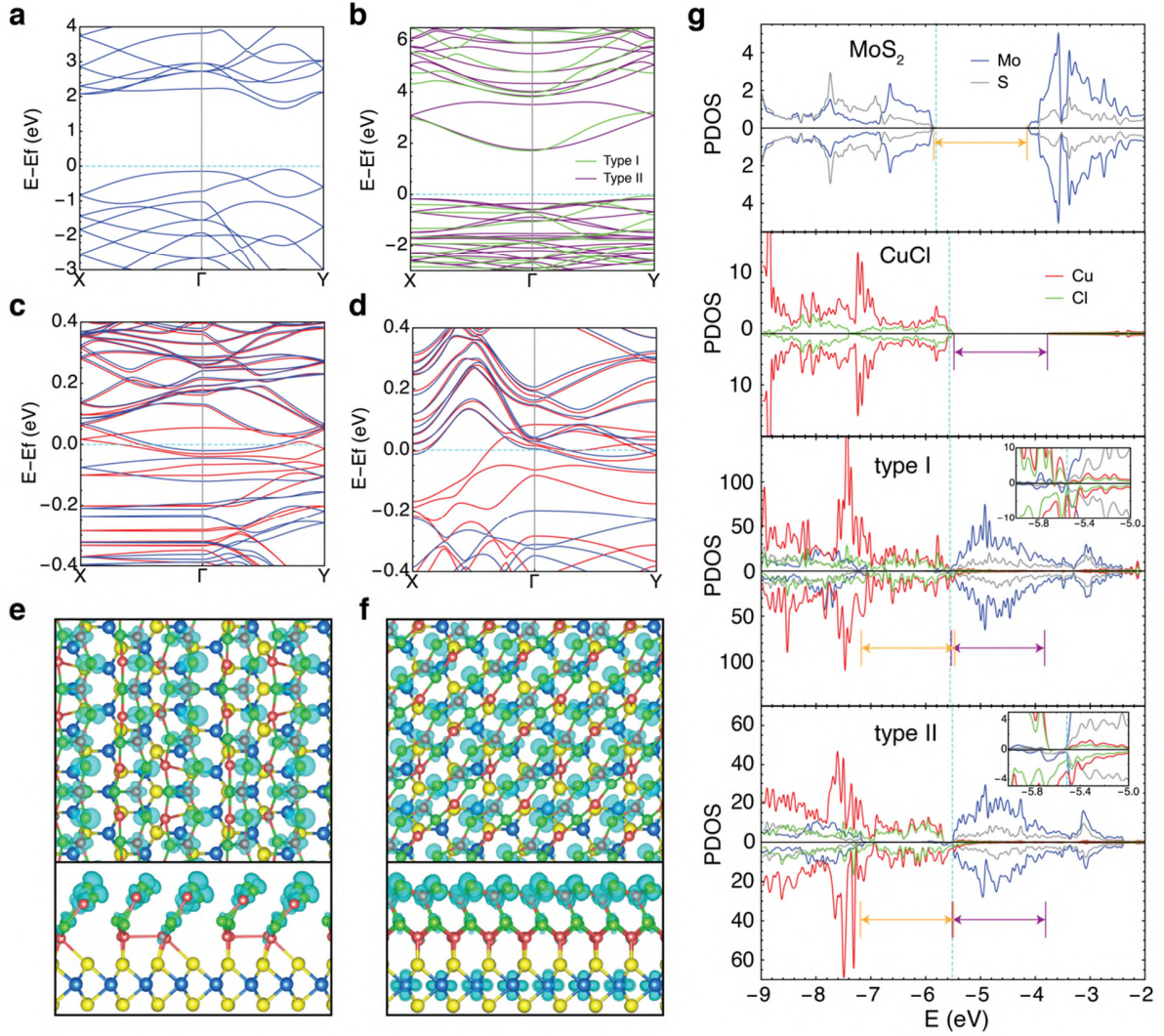


Figure 7. Electronic properties of MoS₂/CuCl heterostructures predicted by DFT simulations. Bandstructures of (a) isolated MoS₂ monolayer, (b) isolated CuCl monolayer with type I and type II alignments, (c) type I and (d) type II MoS₂/CuCl heterostructures, with the Fermi level illustrated by the dashed cyan lines. In panel (c)(d), the spin-up and spin-down components are shown in blue and red, respectively. Partial charge densities of the highest valence bands at Γ point for the (e) type I and (f) type II interfaces. (g) Projected density of states (PDOS) on elements for the isolated MoS₂ monolayer, isolated CuCl monolayer, and two types of MoS₂/CuCl heterostructures. The orange and purple arrows present the

bandgaps of the MoS₂ and CuCl monolayers, and their energy shifts in the presence of the interfaces. The insets show the PDOS around the Fermi levels, which highlight the emergence of mid-gap states.

DFT+U method was employed to qualitatively explore the electronic properties of the two types of favorable MoS₂/CuCl heterostructures identified by experiments. While the bulk MoS₂ and CuCl crystals have indirect and direct band gaps, respectively, the inhomogeneous quantum confinement effects in momentum space turn their monolayer counterparts to be direct and indirect band gap material. As expected from their different symmetry groups, the isolated MoS₂ and CuCl monolayers exhibit distinct dispersion relationships with the band edges located at the K and Γ/Y points (Figure 7a,b), implying that the assistance of phonons is required for the charge transfer between these two domains. In contrast to the type-II interface speculated from the energy levels of individual components, the projected density of states (PDOS) of the combined MoS₂/CuCl systems suggest a type-III alignment with metallic behaviors (Figure 7g). This can be explained by the noticeable shifts of MoS₂ energy levels in the presence of a large dipole moment embedded in the adjacent CuCl crystal, as well as the emergence of additional mid-gap states originating from the strong orbital hybridization between chemically connected sheets. The consequential internal charge transfer from CuCl to MoS₂ in combination with the potential gradient modify the occupations of d-orbitals and lead to the splitting between spin-up and spin-down states (Figure 7c,d). Due to the ionic nature and flexibility of CuCl crystals, the wavefunctions remain delocalized over the entire sheets, even though there exist noticeable distortions at the interface (Figure 7e,f, Supporting information, Figure S18). From the similar PDOS obtained at the two types of interfaces, both energy level alignment and ground state charge distribution are insensitive to the stacking pattern. However, the dynamic processes such as charge hopping, optical excitation and exciton dissociation, may intensively rely on the crystalline alignment, because electron

couplings between the two sheets are sensitive to the wavefunction overlap at the interface, and the tunneling probabilities depend on the alignment in momentum space.

Conclusion

In summary, we showed that 2D ionic CuCl crystals adopt a non-layered cubic zinc-blende crystal configuration on the surface of the MoS₂ monolayers with strong epitaxial correlations between the lattice directions of the two crystals. The generation of 2D CuCl was achieved by simply depositing the CuCl₂ solution onto MoS₂ followed by a proper dose of electron beam irradiation to initiate precursor decomposition and subsequent *in-situ* reactivity. 2D strain maps on CuCl membrane shows a decrease of lattice periodicity as the bulk CuCl is thinned into a 2D form and templated on the substrate with different symmetry. DFT simulations explained the formation of commensurate superlattices *via* bonding pattern matching, and revealed the distinct electronic structures of the MoS₂/CuCl heterostructures compared to their components. These studies provide insights into the generation of more 2D heterostructures with a broader material choice, and show how 2D transition metal dichalcogenides perform as a template to stabilize the non-layered ionic crystal membrane on top through interfacial interactions.

Methods

Synthesis and transfer of MoS₂ monolayers.

Monolayer MoS₂ were grown directly on the SiO₂/Si (300 nm thick SiO₂) substrate by a hydrogen-free chemical vapor deposition method under atmospheric pressure, which is similar as previously

reported work.^{12,30} Molybdenum trioxide (MoO_3 , $\geq 99.5\%$, Sigma-Aldrich) and sulfur (S , $\geq 99.5\%$, Sigma-Aldrich) powder were used as precursors. We loaded MoO_3 powder into a smaller diameter tube ($\sim 1\text{ cm}$) while placed S powder in the outer 1-inch quartz tube, as this will avoid the cross-contamination between two precursors at high temperature. Two furnaces were applied to provide independent temperature control for both two precursors and the substrate. S powder and the substrate were put in the center of the first and second furnace, while MoO_3 powder was positioned at the upstream of the second furnace. The whole growth system was first flushed by the argon gas using a high flow rate for 40 minutes followed by pre-introducing S vapor for ~ 15 min to create a sulfur-sufficient atmosphere. After that, the temperature for the second furnace started to increase to $\sim 800^\circ\text{C}$ at a ramping rate of $40^\circ\text{C}/\text{min}$ and maintained for 15 minutes under 150 sccm argon flow. The argon flow rate was then reduced to 10 sccm and kept for 25 minutes before the growth stopped, followed by a fast cooling process. The temperature for S was retained at $\sim 180^\circ\text{C}$ during the whole synthesis period.

A thin film of poly (methyl methacrylate) (PMMA) was spin coated onto the surface of the $\text{MoS}_2/\text{SiO}_2/\text{Si}$ substrate. The underlying SiO_2 was etched away by floating it on the 1 mol/L potassium hydroxide solution. After it peeled off, the PMMA/ MoS_2 membrane was transferred into the deionized water for three times to wash off residual contamination from the etchant. The film was subsequently scooped up by a quantifoil TEM grid (Agar Scientific AGS175-3). Once left to dry in the air for overnight, the sample was baked on a hot plate at 150°C for 15 minutes to ensure a strong interfacial attachment between MoS_2 monolayers and the quantifoil membrane. Finally, the TEM grid was submerged in acetone for 8 hours to remove the PMMA scaffold.

Transmission electron microscopy and image processing

The AC-TEM was conducted using Oxford's JEOL JEM-2200MCO field emission gun TEM with a CEOS imaging aberration corrector under a low accelerating voltage of 80 kV. AC-TEM Images were captured using a Gatan Ultrascan $4k \times 4k$ CCD camera with 1-2 s acquisition time, 2 pixel binning under the electron dose of $\sim 10^5 e^-/\text{nm}^2$. The pixel resolution for high-magnification AC-TEM images is 145 pixels /nm. ImageJ software was applied to process AC-TEM images. Images were initially adjusted with a band-pass filter (between 100 and 1 pixel) to modify the long-range non-uniformity on the illumination intensity, and then smoothed by applying a Gaussian blur (2-4 pixels). Atomic models were generated using the software of Accelrys Discovery Studio Visualizer. Simulated multislice images based on corresponding atomic models were established *via* JEMS software with a proper parameter adjustment according to the TEM experimental condition. The reconstructed AC-TEM images shown in Figure 2d is constructed by first applying a mask to 2D FFT in Figure 2b to only choose the lattice contribution from MoS₂ and obtaining the reconstructed AC-TEM image. Secondly, overlap Figure 2c, which only includes 2D CuCl lattice, onto this reconstructed AC-TEM having only MoS₂ lattice structure, and use red and green circles to label Cu and Cl atomic positions in Figure 2c. Thirdly, remove Figure 2c to get the image in Figure 2d, where the position of each atom in 2D CuCl crystal with respect to the MoS₂ substrate is clearly revealed. Figure 3f is obtained using the same method. For the line profile in Figure 2i, the intensity at the pristine and heteroepitaxial regions are measured along semitransparent yellow and cyan lines in experimental and simulated TEM images, respectively. Since the atomic column marked as 'A' in Figure 2a and Figure 2f correspond to the lattice structure where the Cu atom from CuCl almost fully overlaps with a double S atoms of monolayer MoS₂, which is confirmed by the analysis in Figure 2d and the atomic model in Figure 2e. It is chosen as a starting point for the intensity measurement in the heteroepitaxial area, because the lattice stacking pattern between

CuCl and monolayer MoS₂ around this point has a good correspondence between AC-TEM image and the image simulation. Therefore, only the thickness of 2D CuCl influences the match of intensity line profiles between the experimental and simulated image. In Figure 3i, a similar approach is used, where two reference points, B and C, are selected.

2D displacement and strain maps

The generation of 2D strain maps in Figure 5(ii) is realized by using a similar real space analysis method as previously reported work.^{31–34} It is based on the generation of 2D displacement maps. We first identified the precise positions of atoms in the 2D CuCl based on the reconstructed AC-TEM images in Figure 6e and j, and then subtracted them from their expected locations in a regular and periodic 2D CuCl lattice. The interplanar spacing of this regular and periodic lattice is set to be the average interplanar spacing of the 2D CuCl nanocrystal in Figure 6e and j, respectively, confirmed by the 2D FFT of corresponding AC-TEM images. After getting the displacement maps of 2D CuCl crystals, we can resolve the 2D local lattice strain through first doing the scattered interpolant on the displacement map with a proper step-size, and then calculating the displacement value difference divided by their location variations along certain directions between each two interpolated spots to form 2D gradient maps of $\partial U_x/\partial x$, $\partial U_y/\partial y$, $\partial U_x/\partial y$ and $\partial U_y/\partial x$. These strain maps could not only show the general lattice distortion but also reveal the level of the structural regularity at different locations in a single 2D CuCl nanocrystal formed on monolayer MoS₂, such as comparing the variations on the bond length or the lattice shear between atomic sites in the crystal centre and close to edges.

Density Functional Theory Calculation

Standard ab-initio calculations within the framework of density-functional theory (DFT) were performed to investigate the microscopic structures and electronic properties of MoS₂/CuCl heterostructures, using the Vienna *Ab Initio* Simulation Package (VASP v5.4).³⁵ Plane-wave and projector-augmented-wave (PAW) type pseudopotentials³⁶ were used, with GGA-PBE exchange-correlation functional³⁷ and a 400 eV kinetic-energy cutoff. The DFT-D3 method of Grimme³⁸ was employed to take the Van der Waals interactions into account, with the cutoff radius for pair interactions set to 50 Å. Dipole correction³⁹ was included to correct the leading errors caused by the large dipole moment in a finite periodic simulation box. A 15 Å vacuum was constructed to avoid fake interactions between periodic images. The structures were relaxed until all forces were smaller than 0.02 eV/Å. For both favorable alignment types identified by experiments, a range of supercells with relatively small lattice mismatches were tested, and the candidates with the highest regularities (type I: MoS₂-3×5, CuCl-4×4, 154 atoms; type II: MoS₂-1×7, CuCl-1×4, 74 atoms) were selected as representatives to explore the electronic properties. The average structures of the nearly degenerate representatives induced by symmetry were used for TEM image simulations. The electronic structures were computed with Monkhorst-Pack k-point grids⁴⁰ of 9×9×1 and 21×6×1 for the two types of heterostructures, respectively. DFT+U method was employed to enhance the electronic correlation,⁴¹ with U=8 eV and J=0.95 eV applied to the Cu d orbitals to correct the energy level of Cu-d band.⁴² We note that given the incapability of DFT to account for many-body effects, the results should be interpreted qualitatively for revealing the impact of heterostructure on electronic properties.

Conflict of Interest: The authors declare no competing financial interest.

Acknowledgements

J.H.W thanks the Royal Society for support. S.W thanks the China Scholarship Council for support. H.L thanks the support from ExxonMobil under the MIT Energy Initiative (Grant EM09079). This research used resources of the National Energy Research Scientific Computing Center, a DOE Office of Science User Facility supported by the Office of Science of the U.S. Department of Energy under Contract No. DE-AC02-05CH11231.

Supporting Information Available: Supplementary figures including atomic models of different possible crystal structures containing element Cu on monolayer MoS₂, TEM image simulations showing the cubic CuCl with different atomic thickness, the influence of defocus values on the imaging of cubic CuCl, the matching level between experimental AC-TEM images and TEM image simulations based on DFT-relaxed CuCl/MoS₂ models, geometric relationship between Type-I and Type-II heteroepitaxy, stacking orientations of thick cubic CuCl on monolayer MoS₂, This material is available free of charge *via* the Internet at <http://pubs.acs.org>.

References

- (1) Kim, K. K.; Hsu, A.; Jia, X.; Kim, S. M.; Shi, Y.; Hofmann, M.; Nezich, D.; Rodriguez-Nieva, J. F.; Dresselhaus, M.; Palacios, T.; Kong, J. Synthesis of Monolayer Hexagonal Boron Nitride on Cu Foil Using Chemical Vapor Deposition. *Nano Lett.* **2012**, *12*, 161–166.
- (2) Kim, S. M.; Hsu, A.; Park, M. H.; Chae, S. H.; Yun, S. J.; Lee, J. S.; Cho, D.-H.; Fang, W.; Lee, C.; Palacios, T.; Dresselhaus, M.; Kim, K. K.; Lee, Y. H.; Kong, J. Synthesis of Large-Area Multilayer Hexagonal Boron Nitride for High Material Performance. *Nat. Commun.* **2015**, *6*, 8662.
- (3) Kang, K.; Xie, S.; Huang, L.; Han, Y.; Huang, P. Y.; Mak, K. F.; Kim, C.-J.; Muller, D.;

- Park, J. High-Mobility Three-Atom-Thick Semiconducting Films with Wafer-Scale Homogeneity. *Nature* **2015**, *520*, 656–660.
- (4) Najmaei, S.; Liu, Z.; Zhou, W.; Zou, X.; Shi, G.; Lei, S.; Yakobson, B. I.; Idrobo, J.-C.; Ajayan, P. M.; Lou, J. Vapour Phase Growth and Grain Boundary Structure of Molybdenum Disulphide Atomic Layers. *Nat. Mater.* **2013**, *12*, 754–759.
- (5) van der Zande, A. M.; Huang, P. Y.; Chenet, D. A.; Berkelbach, T. C.; You, Y.; Lee, G.-H.; Heinz, T. F.; Reichman, D. R.; Muller, D. A.; Hone, J. C. Grains and Grain Boundaries in Highly Crystalline Monolayer Molybdenum Disulphide. *Nat. Mater.* **2013**, *12*, 554–561.
- (6) Geim, A. K.; Grigorieva, I. V. Van Der Waals Heterostructures. *Nature* **2013**, *499*, 419–425.
- (7) Liu, Z.; Song, L.; Zhao, S.; Huang, J.; Ma, L.; Zhang, J.; Lou, J.; Ajayan, P. M. Direct Growth of Graphene/Hexagonal Boron Nitride Stacked Layers. *Nano Lett.* **2011**, *11*, 2032–2037.
- (8) Meng, J. H.; Zhang, X. W.; Wang, H. L.; Ren, X. B.; Jin, C. H.; Yin, Z. G.; Liu, X.; Liu, H. Synthesis of In-Plane and Stacked Graphene/Hexagonal Boron Nitride Heterostructures by Combining with Ion Beam Sputtering Deposition and Chemical Vapor Deposition. *Nanoscale* **2015**, *7*, 16046–16053.
- (9) Shi, Y.; Zhou, W.; Lu, A.-Y.; Fang, W.; Lee, Y.-H.; Hsu, A. L.; Kim, S. M.; Kim, K. K.; Yang, H. Y.; Li, L.-J.; Idrobo, J.-C.; Kong, J. Van Der Waals Epitaxy of MoS₂ Layers Using Graphene as Growth Templates. *Nano Lett.* **2012**, *12*, 2784–2791.

- (10) Zhang, Y.; Shi, J.; Liu, M.; Wen, J.; Ren, X.; Zhou, X.; Ji, Q.; Ma, D.; Zhang, Y.; Jin, C.; Chen, H.; Deng, S.; Xu, N.; Liu, Z.; Zhang, Y. All Chemical Vapor Deposition Synthesis and Intrinsic Bandgap Observation of MoS₂/Graphene Heterostructures. *Adv. Mater.* **2015**, *27*, 7086–7092.
- (11) Latorre-Sánchez, M.; Esteve-Adell, I.; Primo, A.; García, H. Innovative Preparation of MoS₂-Graphene Heterostructures Based on Alginate Containing (NH₄)₂MoS₄ and Their Photocatalytic Activity for H₂ Generation. *Carbon* **2015**, *81*, 587–596.
- (12) Wang, S.; Wang, X.; Warner, J. H. All Chemical Vapor Deposition Growth of MoS₂:h-BN Vertical van Der Waals Heterostructures. *ACS Nano* **2015**, *9*, 5246–5254.
- (13) Fu, L.; Sun, Y.; Wu, N.; Mendes, R. G.; Chen, L.; Xu, Z.; Zhang, T.; Rummeli, M. H.; Rellinghaus, B.; Pohl, D.; Zhuang, L.; Fu, L. Direct Growth of MoS₂/h-BN Heterostructures *via* a Sulfide-Resistant Alloy. *ACS Nano* **2016**, *10*, 2063–2070.
- (14) Gong, Y.; Lin, J.; Wang, X.; Shi, G.; Lei, S.; Lin, Z.; Zou, X.; Ye, G.; Vajtai, R.; Yakobson, B. I.; Terrones, H.; Terrones, M.; Tay, B. K.; Lou, J.; Pantelides, S. T.; Liu, Z.; Zhou, W.; Ajayan, P. M. Vertical and in-Plane Heterostructures from WS₂/MoS₂ Monolayers. *Nat. Mater.* **2014**, *13*, 1135–1142.
- (15) Woods, J. M.; Jung, Y.; Xie, Y.; Liu, W.; Liu, Y.; Wang, H.; Cha, J. J. One-Step Synthesis of MoS₂/WS₂ Layered Heterostructures and Catalytic Activity of Defective Transition Metal Dichalcogenide Films. *ACS Nano* **2016**, *10*, 2004–2009.
- (16) Zhang, J.; Wang, J.; Chen, P.; Sun, Y.; Wu, S.; Jia, Z.; Lu, X.; Yu, H.; Chen, W.; Zhu, J.; Xie, G.; Yang, R.; Shi, D.; Xu, X.; Xiang, J.; Liu, K.; Zhang, G. Observation of Strong Interlayer Coupling in MoS₂/WS₂ Heterostructures. *Adv. Mater.* **2016**, *28*, 1950–1956.

- (17) Yang, W.; Chen, G.; Shi, Z.; Liu, C.-C.; Zhang, L.; Xie, G.; Cheng, M.; Wang, D.; Yang, R.; Shi, D.; Watanabe, K.; Taniguchi, T.; Yao, Y.; Zhang, Y.; Zhang, G. Epitaxial Growth of Single-Domain Graphene on Hexagonal Boron Nitride. *Nat. Mater.* **2013**, *12*, 792–797.
- (18) Yan, A.; Velasco, J.; Kahn, S.; Watanabe, K.; Taniguchi, T.; Wang, F.; Crommie, M. F.; Zettl, A. Direct Growth of Single- and Few-Layer MoS₂ on H-BN with Preferred Relative Rotation Angles. *Nano Lett.* **2015**, *15*, 6324–6331.
- (19) Lin, Y.; Chang, C. S.; Ghosh, R. K.; Li, J.; Zhu, H.; Diaconescu, B.; Ohta, T.; Peng, X.; Lu, N.; Kim, M. J.; Robinson, J. T.; Wallace, R. M.; Mayer, T. S.; Datta, S.; Li, L.-J.; Robinson, J. A. Atomically Thin Heterostructures Based on Single-Layer Tungsten Diselenide and Graphene. *Nano Lett.* **2014**, *14*, 6936–6941.
- (20) Miwa, J. A.; Dendzik, M.; Grønborg, S. S.; Bianchi, M.; Lauritsen, J. V.; Hofmann, P.; Ulstrup, S. Van Der Waals Epitaxy of Two-Dimensional MoS₂ Graphene Heterostructures in Ultrahigh Vacuum. *ACS Nano* **2015**, *9*, 6502–6510.
- (21) Liu, X.; Balla, I.; Bergeron, H.; Campbell, G. P.; Bedzyk, M. J.; Hersam, M. C. Rotationally Commensurate Growth of MoS₂ on Epitaxial Graphene. *ACS Nano* **2016**, *10*, 1067–1075.
- (22) Novoselov, K. S.; Mishchenko, A.; Carvalho, A.; Neto Castro, A. H. 2D Materials and van Der Waals Heterostructures. *Science* **2016**, *353*, aac9439.
- (23) Chen, Q.; He, K.; Robertson, A. W.; Kirkland, A. I.; Warner, J. H. Atomic Structure and Dynamics of Epitaxial 2D Crystalline Gold on Graphene at Elevated Temperatures. *ACS Nano* **2016**, *10*, 10418–10427.

- (24) Al Balushi, Z. Y.; Wang, K.; Ghosh, R. K.; Vilá, R. A.; Eichfeld, S. M.; Caldwell, J. D.; Qin, X.; Lin, Y.-C.; DeSario, P. A.; Stone, G.; Subramanian, S.; Paul, D. F.; Wallace, R. M.; Datta, S.; Redwing, J. M.; Robinson, J. A. Two-Dimensional Gallium Nitride Realized *via* Graphene Encapsulation. *Nat. Mater.* **2016**, *15*, 1166–1171.
- (25) Zhao, J.; Deng, Q.; Bachmatiuk, A.; Sandeep, G.; Popov, A.; Eckert, J.; Rummeli, M. H. Free-Standing Single-Atom-Thick Iron Membranes Suspended in Graphene Pores. *Science* **2014**, *343*, 1228–1232.
- (26) Quang, H. T.; Bachmatiuk, A.; Dianat, A.; Ortmann, F.; Zhao, J.; Warner, J. H.; Eckert, J.; Cuniberti, G.; Rummeli, M. H. In Situ Observations of Free-Standing ZnO Membranes. *ACS Nano* **2015**, *9*, 11408–11413.
- (27) Madelung, O. Semiconductors: Data Handbook. *Springer* **2003**, 911–914.
- (28) Nakayama, M.; Ichida, H.; Nishimura, H. Bound-Biexciton Photoluminescence in CuCl Thin Films Grown by Vacuum Deposition. *J. Phys. Condens. Matter* **1999**, *11*, 7653–7662.
- (29) Robertson, A. W.; Montanari, B.; He, K.; Allen, C. S.; Wu, Y. a.; Harrison, N. M.; Kirkland, A. I.; Warner, J. H. Structural Reconstruction of the Graphene Monovacancy. *ACS Nano* **2013**, *7*, 4495–4502.
- (30) Wang, S.; Rong, Y.; Fan, Y.; Pacios, M.; Bhaskaran, H.; He, K.; Warner, J. H. Shape Evolution of Monolayer MoS₂ Crystals Grown by Chemical Vapor Deposition. *Chem. Mater.* **2014**, *26*, 6371–6379.
- (31) Wang, S.; Lee, G.-D.; Lee, S.; Yoon, E.; Warner, J. H. Detailed Atomic Reconstruction of

Extended Line Defects in Monolayer MoS₂. *ACS Nano* **2016**, *10*, 5419–5430.

- (32) Rasool, H. I.; Ophus, C.; Zhang, Z.; Crommie, M. F.; Yakobson, B. I.; Zettl, A. Conserved Atomic Bonding Sequences and Strain Organization of Graphene Grain Boundaries. *Nano Lett.* **2014**, *14*, 7057–7063.
- (33) Chen, Q.; Robertson, A. W.; He, K.; Gong, C.; Yoon, E.; Lee, G.; Warner, J. H. Atomic Level Distributed Strain within Rotations. *ACS Nano* **2015**, *9*, 8599–8608.
- (34) Warner, J. H.; Young, N. P.; Kirkland, A. I.; Briggs, G. A. D. Resolving Strain in Carbon Nanotubes at the Atomic Level. *Nat. Mater.* **2011**, *10*, 958–962.
- (35) Kresse, G.; Furthmüller, J. Efficient Iterative Schemes for *Ab Initio* Total-Energy Calculations Using a Plane-Wave Basis Set. *Phys. Rev. B* **1996**, *54*, 11169–11186.
- (36) Blochl, P. E. Projector Augmented-Wave Method. *Phys. Rev. B* **1994**, *50*, 17953–17979.
- (37) Perdew, J. P.; Burke, K.; Ernzerhof, M. Generalized Gradient Approximation Made Simple. *Phys. Rev. Lett.* **1996**, *77*, 3865–3868.
- (38) Grimme, S.; Antony, J.; Ehrlich, S.; Krieg, H. A Consistent and Accurate *Ab Initio* Parametrization of Density Functional Dispersion Correction (DFT-D) for the 94 Elements H-Pu. *J. Chem. Phys.* **2010**, *132*, 154104.
- (39) Makov, G.; Payne, M. Periodic Boundary Conditions in *Ab Initio* Calculations. *Phys. Rev. B* **1995**, *51*, 4014–4022.
- (40) Pack, J. D.; Monkhorst, H. J. “Special Points for Brillouin-Zone Integrations”—a Reply. *Phys. Rev. B* **1977**, *16*, 1748–1749.
- (41) Liechtenstein, A. I.; Anisimov, V. I.; Zaanen, J. Density-Functional Theory and Strong

Interactions: Orbital Ordering in Mott-Hubbard Insulators. *Phys. Rev. B* **1995**, 52, 5467–5471.

- (42) Zhou, B.; Dong, S.; Wang, J.; Zhao, H.; Wu, P. Effects of Enhanced Electronic Correlation on Magnetic Properties of Light Non-Metallic Element (B, C, N, and O)-Doped CuCl: A First-Principles Study. *Phys. Lett. A* **2014**, 378, 3001–3005.

TOC graphic

